東京大学 大学院新領域創成科学研究科
基盤科学研究系
先端エネルギー工学専攻

平成 25 年度

修士論文

Surface Temperature Control of TPS Materials by Laser Heating in Plasma Wind Tunnel Experiments

－　アーク加熱風洞試験におけるレーザー照射による熱防御材表面温度制御　－

2014 年 1 月提出
指導教員　小紫　公也　教授

47126058　伊藤　彦

Acknowledgments

First of all, I would like to express my sincerest appreciation to my supervisor, Prof. Kimiya Komurasaki, Department of Advanced Energy, The University of Tokyo. Under his accurate advisement and with his encouragement this thesis was done. Associate Prof. Hiroyuki Koizumi gave me specific advice about spectroscopic experiment. I appreciate his kind help. I also appreciate assistant Prof. Tony Schönherr for his advice and especially great checking and correction of my presentation and thesis.

I further thank to Dr. Georg Herdrich for his invitation to research at Institute of Space Systems, IRS. All of my experiences in Germany were very impressive and interesting. I express here a deep appreciation to all members in IRS.

My special thanks are due to Dr. Satoshi Nomura for guiding my research with detailed comments. Not only during his student year, but also after his graduation, I had been saved by his grand experience and knowledge about the testing facilities.

I want to thank great teammates in our research team. Dr Ai Momozawa provided sample materials for my experiment. Mr. Kaneko and Mr. Yokote also helped my experiments.

Finally but not least I want to thank all laboratory members for comfortable atmosphere and express my best appreciation to my family.

Contents

List of Figures

List of Tables

Nomenclature

A	=	Intensity correction factor
c	=	speed of light
D	=	holder diameter
d	=	sample diameter
H	=	enthalpy
h	=	Plank's constant
I	=	intensity
K	=	integrated absorption coefficient
Kn	=	Knudsen number
k	=	absorption coefficient
$\mathbf{k}$	=	wave vector
k_B	=	Boltzmann constant
M	=	Mach number
m	=	atomic mass
N	=	number density
n	=	refraction index
P	=	probability
p	=	pressure
q	=	heating rate
R	=	gas constant
r	=	laser transmission pass
S	=	surface area
T	=	temperature
W_0	=	beam waste
α	=	a ratio of FWHM of the XBSAS profile to true profile
γ	=	heat capacity ratio
Δd	=	shock stand-off distance
ε	=	emissivity
θ	=	optimum divergence angle
v	=	velocity

$\mathbf{v}$	=	velocity vector
λ	=	wavelength
λ_{mean}	=	mean free path
ν	=	frequency
ρ	=	density
σ	=	Stefan–Boltzmann constant
τ	=	time constant
ω	=	angular velocity

Subscripts

cs	=	cross-beam saturated
D	=	Doppler
L	=	Lorentz
i	=	i-state
j	=	j-state
p	=	probe
S	=	saturated
s	=	stagnation-point
tr	=	Translational
w	=	wall
1	=	upstream of shock wave
2	=	downstream of shock wave

Superscripts

0	=	without absorber

Chapter 1 INTRODUCTION

1.1 Development of Thermal Protection System

Development of Thermal Protection System (TPS) is becoming of great importance for space exploration. TPS has been used to protect space vehicles or sample return capsules which are exposed to severe heat loads by aerodynamic heating during re-entry to the Earth's atmosphere. TPS is roughly classified into two categories; one is reusable and the other is ablative according to the definition of a mission architecture and entry environment. The boundary of two types was fixed by Howe[1]. In the higher re-entry velocity region, there is no material which can overcome the severe heating environment. Thus, only ablative type can be used. For example in the case of Japanese science mission MUSES-C, later on named Hayabusa, the velocity of a re-entry capsule reached to super-orbital (12 km/s) and the total heat flux was estimated over 15 MW/m_2[2]. The capsule which contained asteroid samples was successfully protected by using lattice layered carbon phenolic (LCCP) which is one of the ablative TPSs. During its entry flight, observation from ground based station had been conducted. The surface temperature of the capsule reached a peak of 3250 K when the capsule was at an altitude of 55.95 km[3]. On the other hand, reusable TPS has been studied for manned re-entry vehicles like space shuttle and hypersonic transfer. Nose tips of these were heated up to around 1800 K[4]. Candidates of reusable TPS is required not only high temperature capability, but also enough oxidation resistance. To increase oxidation resistance, silicon carbide (SiC) is adapted for most reusable TPS. Developed materials of each TPS are summarized in Table 1.1[5,6].

Table 1.1 Summary of materials of thermal protection system

TPS materials	PICA	C/C	LCCP	C/C-SiC
Type	Ablative			Reusable
Applied space mission	Stardust	Genesis	Hayabusa	Space shuttle
Relative entry velocity of the mission	12.6 km/s	10.8 km/s	11.3 km/s	7 km/s

Ground test facilities which can simulate re-entry conditions are necessary to develop both type of TPSs, because actual flight-test has many problems such as high cost, less duplicability and restriction of measurement equipments.

1.2 Ground test facilities for TPS development

Re-entry conditions have been reproduced on the ground by using high enthalpy flow generators, such as shock tubes, expansion tubes, shock tunnels and plasma wind tunnels. It is difficult to exactly reproduce the re-entry condition with one type of ground test facility but these facilities cover their weakness each other. For TPS tests, more than several ten minutes of operation time is required to observe the interaction between hot gas and TPS surface. Thus, plasma wind tunnels that have an advantage of their operation time are more suitable for TPS tests[7].

Arc-heated wind tunnels are one of the most widely used plasma wind tunnels[8]. The plasma flow is generated by arc discharge occurring between electrodes. The biggest problem is the contamination of the plasma flow caused by erosion of electrodes. Effective methods to reduce the electrodes have been studied in our laboratory[9]. Despite this disadvantage, various TPS tests have been conducted with arc-heated wind tunnels around the world, and these studies are summarized in Table 1.2. They have mainly focused on the oxidation behavior of TPS. In Japan, most research have focused on ablative type TPS. In the case of ablative type, oxidation behavior depends on each structure of materials. On the other hand, oxidation behavior of reusable type is determined primarily by oxidation behavior of adopted SiC. Thus, understanding the oxidation behavior of SiC is of paramount importance to develop the reusable type TPS.

Table 1.2 Summary of arc-heated wind tunnels in the world

County	**Facility**	**Type**	**Tested TPS materials**	**Total pressure, MPa**	**Specific enthalpy, MJ/kg**	**Reference**
USA	AHF	Segment	PICA, C/C, ZrB_2-SiC, HfB_2-SiC	1	32.5	[10,11]
	IHF	Segment	LCCP	1	46.4	[12]
Germany	L2K	Huels	ZrB_2-SiC	1.4	20	[13]
	PWK2	MPD	AQ60, C/C-C/SiC	0.1	150	[14,15]
Italy	Federico 2	Electronic	ZrB_2-SiC	1.1	10	[16]
Japan	AWT (ISAS)	Segment	LCCP, C/C-C/SiC	0.1	20	[15,17]

1.3 Oxidation behavior of SiC

SiC is expected to be structural material at high temperature because of their superior chemical and physical stability and mechanical properties. Moreover, it is known to have excellent high-temperature oxidation performance. SiC exhibits two types of oxidation behavior, active and passive oxidation, depending on oxygen partial pressure and temperature[18]. Active oxidation occurs under low oxygen partial pressure and high temperature. In active oxidation, SiC evaporates by the formation of SiO and CO gaseous. Active oxidation reaction with oxygen gas can be expressed by Equation (1.1).

$$SiC(s) + O_2(g) \rightarrow SiO(g) + CO(g) \quad (1.1)$$

In contrast passive oxidation is observed at high oxygen pressure and low temperature, in which a protective SiO_2 film prevents further oxidation (Equation (1.2))

$$SiC(s) + 3/2O_2(g) \rightarrow SiO_2(s) + CO(g) \quad (1.2)$$

Schematic of active/passive oxidation is shown in Figure 1.1. Consequently, SiC is useful for TPS only in the passive oxidation conditions and investigation of the transition condition of active/passive oxidation transition (A/P-T) is of great importance. Several researchers have studied A/P-T condition and Kubota reviewed their recent research[19]. The border of A/P-T condition is reported within 1600 to 2000 K. He argued that the large scattering of A/P-T condition is provided by different configuration of the experimental devices and direction of the transition. To define the A/P-T condition, more detailed study and sophisticated numerical models are required.

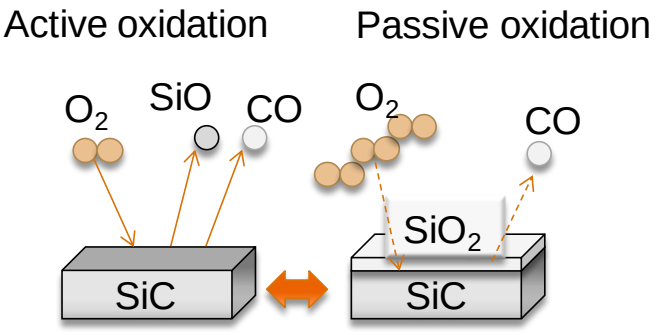

Figure 1.1 Schematic of active/passive oxidation

1.4 Application of arc-heated wind tunnel for TPS development

Most of studies about oxidation behavior of SiC have been conducted with thermogravimetric or actinometric apparatus[20,21,22]. These apparatus enable us to control temperature of specimen and oxygen partial pressure independently. It also can provide contamination-free plasma. However, there is a criticism that oxygen partial pressure in these facilities should distribute around the specimen due to conventional diffusion and it should be taken into account. To consider the conventional diffusion effect, tests with dynamic plasma flow and investigations of the plasma flow are strongly required.

Although many research groups have tested TPS materials in which SiC is contained, as shown in previous table, A/P-T condition of SiC had not been studied yet by arc-heated wind tunnel. In their experiments, oxidation behavior is surveyed into heat flux and total pressure. But the problem is that independently control of each parameter is impossible at arc-heated wind tunnel experiment. These parameters are determined by a lot of flow parameters such as Mach number, specific enthalpy, gas composition and plasma temperature. However, the flow condition of arc-heated wind tunnel is controlled by only two parameters, input power and gas flow rate. This makes the investigation of A/P-T condition difficult. To research A/P-T condition by arc-heated wind tunnel, the independent controlled of gas pressure and specimen temperature at 1600 to 2000 K is required.

1.5 Shock layer measurement by Cross-beam Saturated Absorption Spectroscopy

For the determination of oxidation rate of SiC, not only the temperature of a specimen but also the gas temperature around a specimen is considered as an important factor. When a sample probe is set in supersonic plasma flow, shock layer occurs in front of the probe. Thus shock layer measurement of plasma flow is strongly required. A lot of plasma diagnostic techniques have been developed and these techniques are classified into intrusive and non-intrusive methods. For shock layer measurement, non-intrusive methods such as spectroscopic methods are more suitable than intrusive. Mainly three spectroscopic methods have been applied to the plasma wind tunnel flow, optical emission spectroscopy (OES), laser absorption spectroscopy (LAS) and laser-induced fluorescence (LIF). OES enable us to figure out lots of information such as translational, rotational, vibrational and electronic excitation temperatures and it has been applied to shock layer measurement. Although emission spectroscopy has been employed as a powerful tool to obtain molecular spectra and intensity of atomic line spectra or to identify the chemical composition, its

wavelength resolution is limited to sub-nanometer. In plasma wind tunnel flow the atomic line broadening is in the order of picometer and cannot be resolved by emission spectroscopy. For the evaluation of atomic line broadening the narrow band laser spectroscopy is required. LIF and LAS have been applied to resolve an atomic absorption profile. LAS is a powerful tool to measure translational temperature but the problem is that LAS is one of line-of-sight measurements and it cannot be applied to shock layer measurement. LIF has an advantage in the possibility of point measurement. However, as mentioned in the references, it is also impossible to measure optically thick shock layer because laser absorption is shifted to the blue side and the fluorescence re-absorption is shifted to the red side[23].

Recently, for point measurement of translational temperature, cross-beam saturated absorption spectroscopy (XBSAS) was developed and applied to shock layer measurement in our laboratory[23]. The distribution of translational temperature on the stagnation streamline was obtained across the shock wave which was generated with 25 mm sphere, shown in Figure 1.2. The peak temperature was 5470±200 K at x=-2.5 mm. This peak is considered as the crossing point of shock layer and thermal boundary layer. From an aspect of study about shock layer structure, translational temperature measurement in shock layer with changing boundary temperature is of great interest.

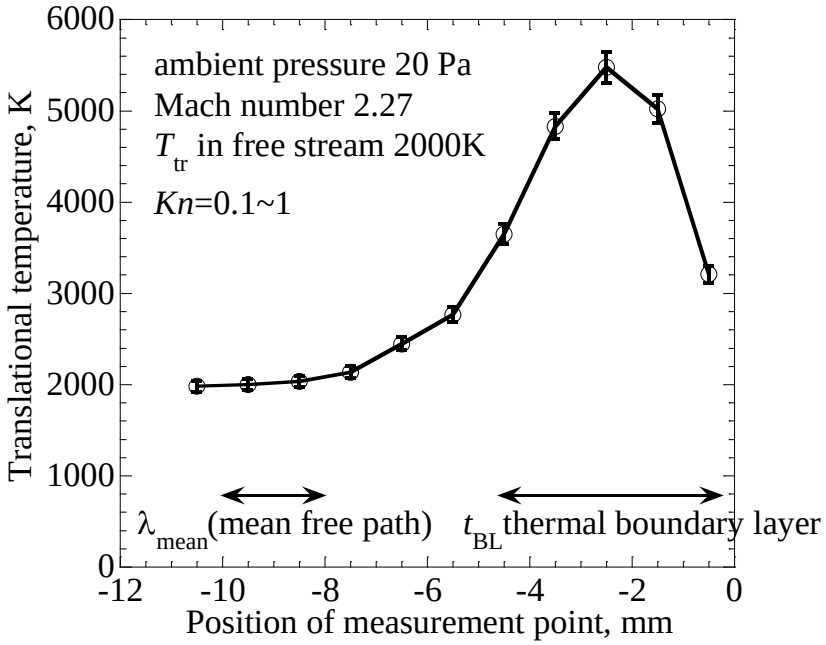

Figure 1.2 Axial distribution of translational temperature in front of the probe with scales of mean free path and thermal boundary layer[23]

1.6 Objectives

In the aforementioned background, independent controlled of gas pressure and surface temperature of a specimen in arc-heated wind tunnel experiment is strongly required from an aspect of TPS development. Moreover, translational temperature measurement in shock layer with changing boundary temperature is of great interest from the point of view of the thermal structure in shock layer. Objectives of this thesis are set as follows,

1. Controlling the surface temperature of a sample probe independently in arc-heated wind tunnel test.

   External heating system using semiconductor laser was installed in 1 kW-crass arc-heated wind tunnel and surface temperature of a sample was successfully controlled independently from plasma flow condition.

2. Translational temperature measurement in front of shock layer with changing boundary temperature.

   Translational temperature distribution in shock layer, which is occurred in front of a sample probe, with changing boundary temperature was measured by XBSAS.

Chapter 2 THEORIES

2.1 Concept of external laser heating system

2.1.1 External laser heating application in ISAS

The concept of external laser heating system in arc-heated wind tunnel is simple; adding heat flux by installing laser beam on a sample surface from the side of plasma flow. In ISAS (Institute of Space and Astronautical Science), 500 W continuous YAG laser is installed on arc-heated wind tunnel[24,25]. Schematic of the system is shown in Figure 2.1. The augmented radiative heat flux by laser irradiation exerts 3 to 4 MW/m_2 on 10 mm by 10 mm area. The wavelength is 1064 nm. Laser beam is directed into the test chamber through quartz window. Details of this system are not reported in the above references.

In this study, the concept is same but an external laser heating system is developed independently from ISAS's. Moreover, this study focuses on not increasing heat flux but controlling surface temperature of a sample in plasma flow. For this purpose, not only laser heating system, but also sample holder is developed considering heat balance. Once a suitable sample holder is designed, various samples can be tested at the same condition.

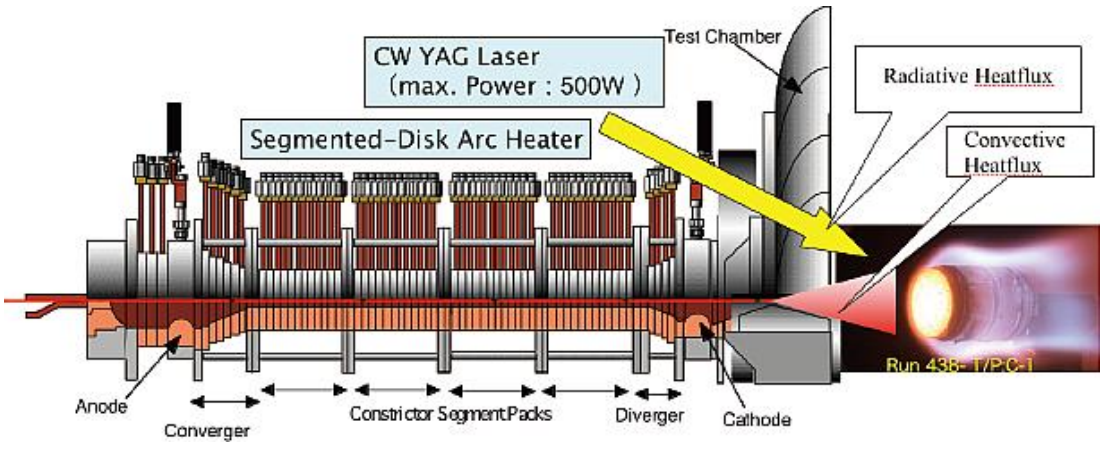

Figure 2.1 Schematic of laser heating system in ISAS[25]

2.1.2 Interaction between argon plasma flow and external semiconductor laser

When a laser frequency corresponds to the absorption line between two energy levels of transmitted plasma particles, the laser beam is absorbed by the plasma. According to the Beer-Lambert law, the absorption, *dI*, is proportional to the optical length, *dx* as shown in Equation (2.1).

$$dI = -kIdx \tag{2.1}$$

Here *k* is the absorption coefficient. Integration of the absorption coefficient from *-r* to *r* along the laser pass is written as

$$-\ln\left(\frac{I_{\mathrm{p}}}{I_{\mathrm{p0}}}\right) = \int_{-r}^{r} k(x)dx \tag{2.2}$$

.

where I_{p} and I_{p0} are incident laser intensity and transmitting laser intensity. In our system, spectral width of semiconductor laser is narrow; full width at half maximum (FWHM) is 3,9 nm. Because argon atom and oxygen atom have no strong absorption line which matches with the laser wavelength, laser absorption of the semiconductor laser is negligibly small.

In addition, the spectrum of argon plasma flow is compared to the spectrum when semiconductor laser transmit the flow. Only one order smaller fluctuation of line intensity compared to ordinary is observed but it is same order as small fluctuation of plasma flow. From the above described discussion, it is concluded that the interaction between argon plasma flow and external semiconductor laser is negligible.

2.1.3 Surface temperature estimation by measured spectrum

The estimation of the surface temperature of a sample in argon plasma flow is performed by fitting theoretical Planck radiation curve to measured spectra from the sample surface. Considering the intensity dependency on spectrometer and emissivity of material, for a wavelength λ, the Planck radiation can be described as Equation (2.3).

$$B_{\lambda}(T) = \frac{2hc^2}{\lambda^5}\frac{A}{e^{\frac{hc}{\lambda k_B T}} - 1} \tag{2.3}$$

Here *A*, *c*, *h*, k_B, *T*, is intensity correction factor, the speed of light, Plank's constant, Boltzmann constant, temperature respectively. Fitting is carried out by Equation (2.3) as a function of λ using least-square method, where *A* and *T* were fitting parameters. Strictly speaking, this fitting method only can apply to a black body because emissivity of every material has own wavelength dependency and temperature dependency. However, in this thesis, measured wavelength range is 650

to 950 nm and this range can show only narrow slope deviated from the peak of Plank radiation. Thus a black body can be assumed for all materials.

2.2 Principle of atomic line broadenings

2.2.1 Homogeneous and inhomogeneous broadenings

Absorption profile of atomic line is broadened by different kinds of mechanism such as thermal motion of atoms, pressure, electric field and magnetic field. When the probability of transition is equal for all atoms, the broadening of this transition profile is called as the homogeneous broadening. The broadenings oriented by pressure, electric field and magnetic field are the homogeneous broadenings. On the other hand, when the transition probability is dependent on atoms, the spectral width is termed as an inhomogeneous broadening. Only Doppler broadening which is oriented by thermal motion belongs to the inhomogeneous broadening. The homogeneous and inhomogeneous broadenings are respectively expressed by Lorentz and Gaussian functions. The broadenings are summarized in Table 2.1. Generally the profile is a convolution of these broadenings and represented by a Voigt function. In plasma wind tunnel measurements usually Doppler broadening is larger than other broadenings by three orders of magnitude approximately[26]. Thus the profile is evaluated by a Gaussian function and the translational temperature is deduced from the broadening.

Table 2.1 Summary of Broadenings.

Broadening	**Origin**	**Line shape function**
Pressure	Collision	Lorentz
Stark	Electric field	Lorentz
Zeeman	Magnetic field	Lorentz
Natural	Finite time of transition	Lorentz
Doppler	Thermal motion of atoms	Gauss

2.2.2 Doppler broadening

The absorption frequency of atoms which have a velocity vector, $\mathbf{v} = \{v_x, v_y, v_z\}$ is shifted because of the Doppler effect as

$$\nu = \nu_0 + \frac{1}{2\pi}\mathbf{k}\cdot\mathbf{v}. \tag{2.4}$$

Here ν, ν_0, and $\mathbf{k}$ respectively denote the absorption frequency, center frequency of absorption, and wave vector. When the laser propagates along the x-axis, i.e. $\mathbf{k} = \{k_x, 0, 0\}$, the absorption frequency of the atoms is

$$\nu = \nu_0\left(1 + \frac{v_x}{c}\right), \tag{2.5}$$

where c is the speed of light. Assuming that the velocity distribution of the atom obeys to the Maxwell distribution, the probability of the velocity component to the light direction is expressed as

$$p(\nu)d\nu = \left(\frac{m}{2\pi k_B T_{tr}}\right)^{1/2}\exp\left(-\frac{m\nu^2}{2k_B T_{tr}}\right)d\nu \tag{2.6}$$

Here m and T_{tr} are mass of the atom and translational temperature respectively. The most probable velocity is a function of translational temperature expressed as,

$$v_p = \sqrt{\frac{2k_B T_{tr}}{m}} \tag{2.7}$$

Here v_p is the most probable velocity. Thus, the number density of atoms with a velocity component between v_x and $v_x + dv_x$

$$n_i(v_x)dv_x = \frac{N_i}{v_p\sqrt{\pi}}\exp\left[-\left(\frac{v_x}{v_p}\right)^2\right]dv_x \tag{2.8}$$

Substituting Equation (2.10) into Equation (2.13), the number density of atoms which absorbs the laser with frequency ν can be expressed as follows.

$$n_i(\nu)d\nu = N_i\frac{c}{\nu_0 v_p\sqrt{\pi}}\exp\left[-\left(\frac{c(\nu-\nu_0)}{\nu_0 v_p}\right)^2\right]d\nu \tag{2.9}$$

Absorption coefficient is proportional to number density of absorbing particles, so the absorption coefficient is expressed as

$$k(\nu) = K_i\frac{2\sqrt{\ln 2}}{\sqrt{\pi}\Delta\nu_D}\exp\left[-\left(\frac{(\nu-\nu_0)}{\Delta\nu_D/2\sqrt{\ln 2}}\right)^2\right] \tag{2.10}$$

Here K_i and $\Delta\nu_D$ are the integrated absorption coefficient and FWHM of the Gaussian profile. This broadening is called the Doppler broadening. Thus $\Delta\nu_D$ is related to T_{tr} as follows.

$$\Delta\nu_D = \frac{2\nu_0\sqrt{\ln 2}}{c}\sqrt{\frac{2k_B T_{tr}}{m}} \tag{2.11}$$

In the application of plasma wind tunnel measurement, $\Delta\nu_D$ ranges from 1 GHz to 10 GHz. This corresponds to the wavelength of 2~20 pico meter. Hence, it is difficult to spectrally resolve a Doppler broadened profile with a spectrometer. In laser spectroscopy if the spectral width of light source is much narrower than $\Delta\nu_D$ it is possible to evaluate the broadening accurately.

2.2.3 Convolution of homogeneous and inhomogeneous broadenings

In general, the profile is a convolution of homogeneous and inhomogeneous broadened profiles. The total absorption coefficient is

$$k(\nu) = K_i \frac{\sqrt{\ln 2}}{\pi^{3/2}} \frac{\Delta\nu_L}{\Delta\nu_D} \int_{-\infty}^{\infty} \frac{\exp\left\{-\left(\nu_\xi - \nu_0\right)^2 / \left(\Delta\nu_D / 2\sqrt{\ln 2}\right)^2\right\} d\nu_\xi}{\left(\nu - \nu_\xi\right)^2 + \left(\Delta\nu_L / 2\right)^2}. \tag{2.12}$$

where $\Delta\nu_L$ is Lorentzian width. This function is called as a Voigt function. This cannot be expressed in closed form and has to be calculated numerically. A number of investigations on the Voigt function have been published and pseudo-Voigt function has been developed for a simple calculation with closed form[27,28].

2.2.4 Absorption saturation

When a transmitted laser frequency matches with the absorption line between two energy levels, the lower state atoms are excited to the upper state by absorbing laser. The number of atom in the lower state n_i is usually smaller than that of atom in upper state n_j but when the laser intensity is high, n_j increases and become close to n_i as shown in Figure 2.2.

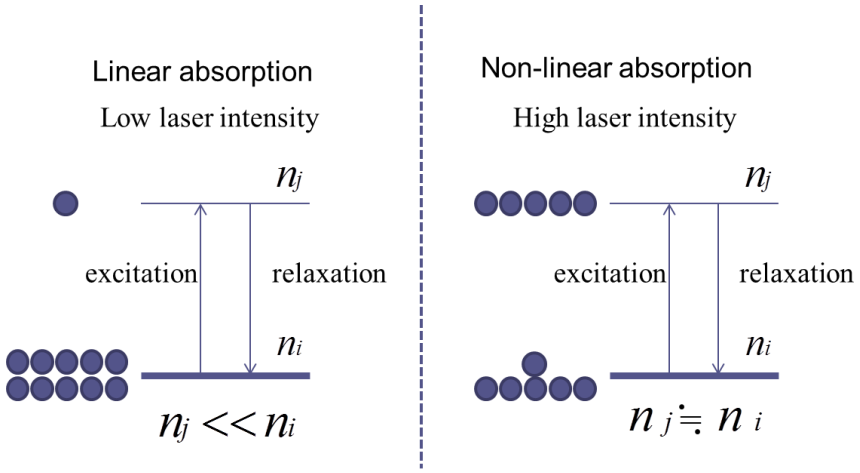

Figure 2.2 Absorption saturation in LAS.

In the former case, absorption signal increase in proportion to the laser intensity but later case absorption signal cannot increase in proportion to the laser intensity, therefore absorption profile is distorted. The effect of absorption saturation in LAS is studied by Matsui[29]. When the inhomogeneous broadening is much more dominant than the homogeneous broadening, in the conventional theory, the saturated absorption coefficient of absorption profile is expressed as

$$k_s(\nu) = K_i \frac{2\sqrt{\ln 2}}{\pi^{3/2}} \frac{\Delta\nu_L}{\Delta\nu_D} \int_{-\infty}^{\infty} \frac{\exp\left\{-\left[2\left(\nu_\xi - \nu_0\right)/\Delta\nu_D\right]^2 \ln 2\right\} d\nu_\xi}{\left(\nu - \nu_\xi\right)^2 + \left(\Delta\nu_L\sqrt{1+I/I_S}\,/2\right)^2} \tag{2.13}$$

Here, I_S is saturation laser intensity. As you can see from the Equation (2.13), the Doppler width is independent of laser intensity, whereas the Lorentzian width increases with laser intensity.

$$\Delta\nu_{SL} = \Delta\nu_L\sqrt{1+I/I_S} \tag{2.14}$$

Then, the relationship between saturated integrated absorption coefficient K_s and K_i is expressed as

$$K_s = \int k_s(\nu)d\nu = K_i\sqrt{1+I/I_S} \tag{2.15}$$

When the pressure broadening is dominant among the homogeneous broadening, I_S is a function of

Root-mean-square velocity $\bar{v}$ and in thermal equilibrium, $\bar{v}$ is defined as

$$I_S \propto \bar{v}(\nu) = \sqrt{\frac{3k_B T_{tr}}{m}} \tag{2.16}$$

As shown in Equation (2.5), the atoms whose absorption frequency is far away from the center have a large velocity component in the laser propagation direction. Thus, Root-mean-square velocity is a function of absorption frequency.

$$\bar{v}(\nu) = \sqrt{(\nu - \nu_0)^2 \frac{c^2}{\nu_0^2} + \frac{2k_B T_{tr}}{m}} \tag{2.17}$$

The modified saturation laser intensity with respect to the velocity distribution $I_s(\nu)$ expressed as

$$I_S(\nu) = I_S \sqrt{\frac{8\ln 2}{3} \frac{(\nu - \nu_0)^2}{\Delta\nu_D{}^2} + \frac{2}{3}} \tag{2.18}$$

This means that the saturation laser intensity around the profile's wing is higher than that near the absorption center line.

2.3 Principle of Cross-beam Saturated Absorption Spectroscopy

2.3.1 Deviation of absorption coefficient at the crossing point

Figure 2.3 shows the schematic of XBSAS. A probe beam with low intensity crosses with a saturating beam which has high intensity. In this thesis, the same light source is used for the probe beam and saturating beam and the both beams have an identical wavelength. Here the axisymmetric distribution is considered for simplicity; however the following derivation is valid also for arbitrary distribution. Without the saturating beam absorbance is the integration of absorption coefficient is expressed as Equation (2.2). When the saturating beam crosses with the probe beam at $x=x_0$ with a small width of Δx, the partly saturated absorbance is described as

$$-\ln\left(\frac{I_{ps}}{I_{p0}}\right) = \int_{-R}^{x_0-\Delta x/2} k dx + \int_{x_0-\Delta x/2}^{x_0+\Delta x/2} k_{cs} dx + \int_{x_0+\Delta x/2}^{R} k dx \tag{2.19}$$

.

I_{ps} is the transmitted probe beam intensity which crosses with the saturating beam. k_{cs} is the cross-beam saturated absorption coefficient. Subtracting Equation (2.19) from Equation (2.2), the information at the crossing point can be extracted as follows.

$$-\ln\left(\frac{I_{\mathrm{p}}}{I_{\mathrm{ps}}}\right)=\left\{k\left(x_0\right)-k_{\mathrm{cs}}\left(x_0\right)\right\}\Delta x \tag{2.20}$$

Here, $k(x)$ is assumed to be uniform in the crossing area. The fluorescence induced by the saturating beam can be neglected because its intensity is much smaller than the probe beam intensity.

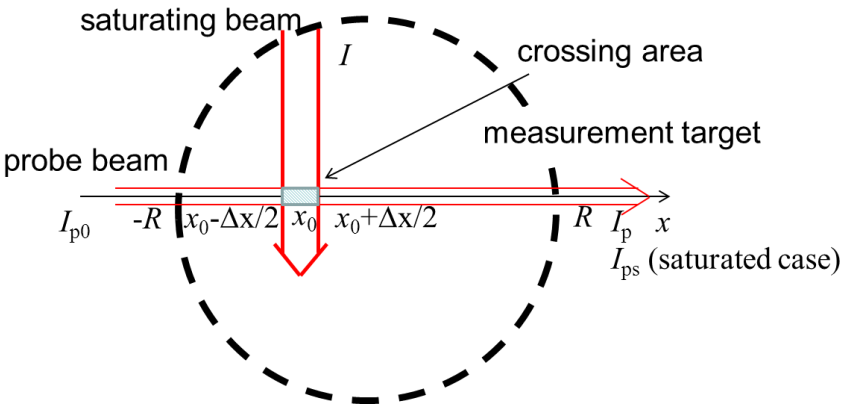

Figure 2.3 Schematic of cross-beam saturated absorption spectroscopy.

In most cases, difference between I_{p} and I_{ps} is so small that it is difficult to deduce $k(x_0)$-$k_{\mathrm{s}}(x_0)$ from $-\ln(I_{\mathrm{p}}/I_{\mathrm{ps}})$ by measuring I_{p} and I_{ps} independently. Thus a phase sensitive detection system was implemented. When the saturating beam intensity is modulated with a switching system, the probe laser intensity shows the oscillating signal as shown in Figure 2.4. In fact, the oscillating signal is not distinguishable from the noise. By using a lock-in-amplifier, only the oscillation which has the modulation frequency can be extracted. The output of the lock-in-amplifier is the oscillation's effective amplitude. Thus it is useful to express Equation (2.20) with ΔI ($=I_{\mathrm{p}}$-I_{ps}). When x is much smaller than unity, $\ln(1+x)$ can be approximated by x. Thus Equation (2.20) can be rewritten as

$$-\frac{\Delta I}{I_{\mathrm{ps}}}=\left\{k\left(x_0\right)-k_{\mathrm{cs}}\left(x_0\right)\right\}\Delta x \tag{2.21}$$

.

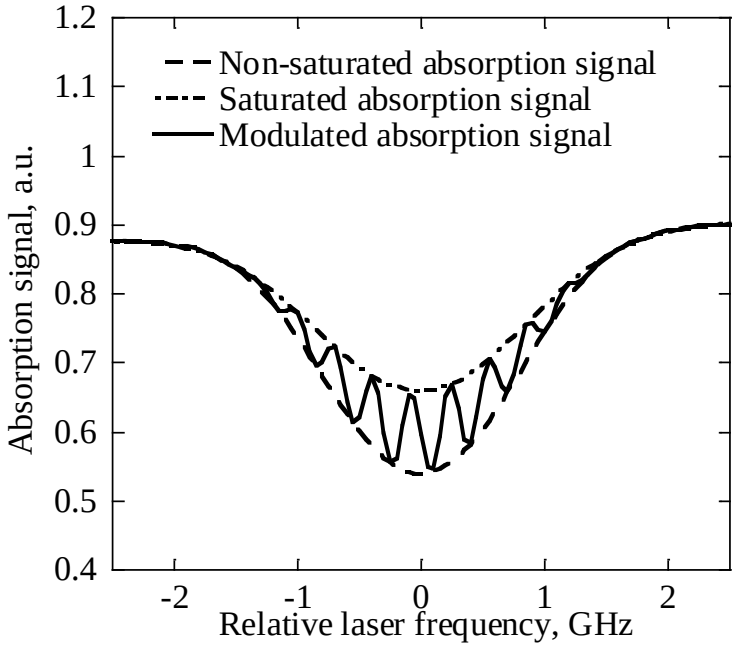

Figure 2.4 Schematic of saturated and unsaturated absorption signals.

2.3.2 Absorption coefficient and translational temperature in XBSAS

The probe beam and saturating beam respectively propagate in the direction of x and y axis with the same frequency. When the laser with a frequency of $\nu_0+\Delta\nu$ transmits the plasma, only the atoms with a velocity component of $(\Delta\nu/\nu_0)c$ in the direction of laser propagation, absorbs the laser. In the single laser absorption spectroscopy, the absorption represents the velocity distribution function along the laser pass and in thermal equilibrium state, a Maxwellian velocity distribution yields the line-shape of the Gaussian function. Meanwhile, in the cross-beam laser absorption spectroscopy, the atom which absorbs the both of probe and saturating beam, must have the same velocity component in the direction of x and y axis. Absorption coefficient can be divided into two groups as Equation (2.22). One is the group in which atoms have the same velocity components for x and y direction, and in the other group the velocity differs for x and y direction.

$$k(\nu) = K_i \times \frac{\sqrt{2\ln 2}}{\pi^{3/2}} \frac{\Delta\nu_L}{\Delta\nu_D} \int_{-\infty}^{\infty} \frac{\exp\left\{-\left(\nu_\xi - \nu_0\right)^2 / \left(\Delta\nu_D / 2\sqrt{\ln 2}\right)^2\right\} \times \alpha d\nu_\xi}{\left(\nu - \nu_\xi\right)^2 + \left(\Delta\nu_L / 2\right)^2}$$
$$+ K_i \times \frac{\sqrt{2\ln 2}}{\pi^{3/2}} \frac{\Delta\nu_L}{\Delta\nu_D} \int_{-\infty}^{\infty} \frac{\exp\left\{-\left(\nu_\xi - \nu_0\right)^2 / \left(\Delta\nu_D / 2\sqrt{\ln 2}\right)^2\right\} \times \{1-\alpha\} d\nu_\xi}{\left(\nu - \nu_\xi\right)^2 + \left(\Delta\nu_L / 2\right)^2} \tag{2.22}$$
$$\alpha = \exp\left\{-\left(\nu_\xi - \nu_0\right)^2 / \left(\Delta\nu_D / 2\sqrt{\ln 2}\right)^2\right\}$$

In cross-beam saturated absorption coefficient only the first term is saturated. The absorption coefficient difference between non-saturated case and cross-beam saturated case is expressed as

$$k(\nu) - k_{\mathrm{cs}}(\nu) = K_i \frac{\sqrt{2\ln 2}}{\pi^{3/2}} \frac{\Delta\nu_L}{\Delta\nu_D} \{ \int_{-\infty}^{\infty} \frac{\exp\left\{-2\left(\nu_\xi - \nu_0\right)^2 / \left(\Delta\nu_D / 2\sqrt{\ln 2}\right)^2\right\} d\nu_\xi}{\left(\nu - \nu_\xi\right)^2 + \left(\Delta\nu_L / 2\right)^2}$$
$$- \int_{-\infty}^{\infty} \frac{\exp\left\{-2\left(\nu_\xi - \nu_0\right)^2 / \left(\Delta\nu_D / 2\sqrt{\ln 2}\right)^2\right\} d\nu_\xi}{\left(\nu - \nu_\xi\right)^2 + \left(\Delta\nu_L \sqrt{1 + I / I_{\mathrm{s}}(\nu)} / 2\right)^2} \} \tag{2.23}$$

In completely saturated region, Equation (2.23) can be written as

$$k(\nu) - k_{\mathrm{cs}}(\nu) = K_i \frac{\sqrt{\ln 2}}{\pi^{3/2}} \frac{\Delta\nu_L}{\Delta\nu_D} \int_{-\infty}^{\infty} \frac{\exp\left(-2\left(2\sqrt{\ln 2}\nu / \Delta\nu_D\right)^2\right) d\nu_\xi}{\left(\nu - \nu_\xi\right)^2 + \left(\Delta\nu_L / 2\right)^2}. \tag{2.24}$$

This function can be seen as a Voigt function whose Doppler broadening is $\Delta\nu_D / \sqrt{2}$. In this case, translational temperature can be obtained by following Equation (2.24).

$$T_{\mathrm{tr}} = \frac{mc^2}{8\ln 2 k_B \nu_0^{\ 2}} \Delta\nu_{D\_\mathrm{XBSAS}}^2 \tag{2.25}$$

When saturation is insufficient, Equation (2.24) is written as

$$T_{\mathrm{tr}} = \frac{mc^2}{4\ln 2 k \nu_0^{\ 2}} \left(\frac{1}{\alpha} \Delta\nu_{D\_\mathrm{XBSAS}}\right)^2. \tag{2.26}$$

where α is a ratio of FWHM of the XBSAS profile to true profile. In this study, α is estimated as 0.69. The estimation method is discussed in Appendix 1.

Chapter 3 EXPERIMENTAL APPARATUS

3.1 Laser heating and surface temperature measurement setup

Laser heating and surface temperature measurement setup is shown in Figure 3.1. As power source a water-cooled semiconductor laser is used. The laser is fed through a multi-mode fiber and was irradiated by collimator. The beam diameter is 6.6 mm, and it is focused on the sample by a lens. The collimated laser beam is transmitted through the quartz window and is focused on the sample inside the vacuum chamber. The reflection caused by the quartz window is measured by a power meter. Using a two-lens system, radiation is concentrated onto the entrance of a circular fiber optic with a diameter of 600 μm. A single line CCD (2048 pixels) spectrometer with a fixed grating is used for detection. Photograph and specification of the spectrometer are shown in Figure 3.2 and Table 3.1. Intensity and wavelength calibration are conducted respectively by using Tungsten-Halogen lamp (Optronic Laboratories Inc. OL 245C) and mercury lamp. The measured spectra range is from 650 to 950 nm as a short pass filter (Thorlabs Inc. FES0950) is used for eliminate the strong diffuse light of the semiconductor laser.

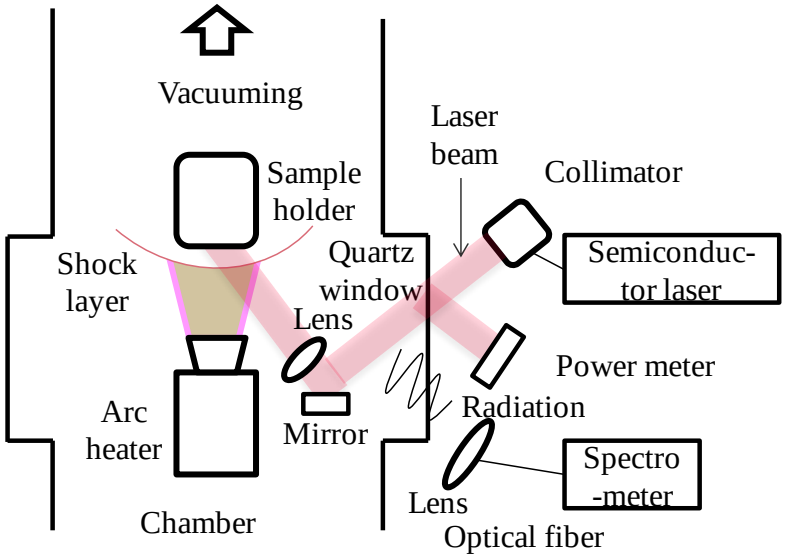

Figure 3.1 Laser heating and surface temperature measurement setup

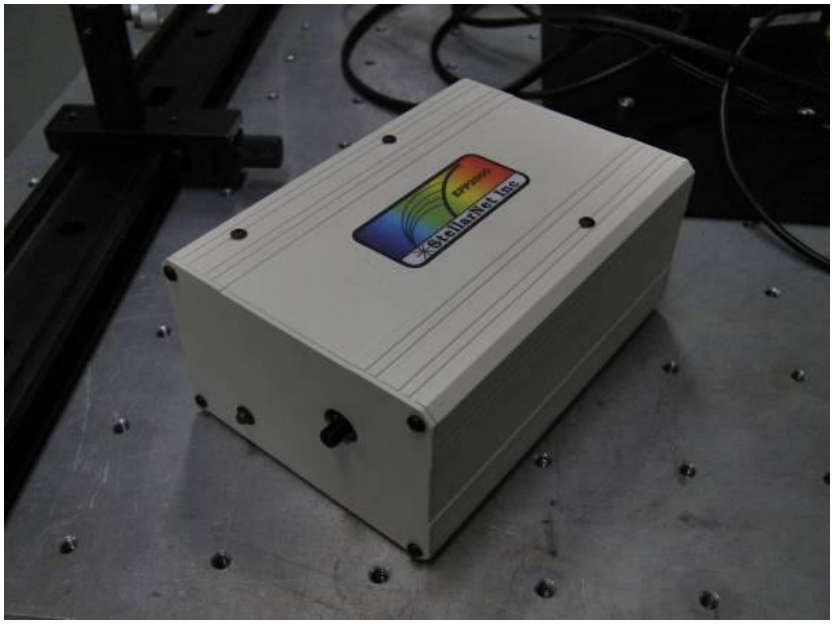

Figure 3.2 Photograph of the spectrometer

Table 3.1 Specification of the spectrometer

Detector range	200-1100 nm
Detector integration	1 ms to 65 s
Resolution	0.75 nm
Fiber optic input	SNA905 single fiber
Fiber NA	0.22

3.2 Semiconductor laser

The specification of semiconductor laser (JEOPTIC Inc. JOLD-250-CPXF-2P2) is shown in Table 3.2. For combining laser beam and optical fiber, optical system is incorporated. Thus laser beam can be irradiated in any direction easily by connecting a fiber. For teaching and targeting purposes before laser operation, pilot laser is mounted and its wavelength is 650 nm. To prevent deterioration of semiconductor element, laser is cooled by water. A chiller (SMC Inc. HRS024-A-20-T) is equipped. The temperature of the water is monitored by measuring the resistance value of a thermometric resister, PT 100. Between PT 100 and a power source (UNITAC Inc. NJLT087) interlock control circuit is arranged. When the water temperature exceeds a limit

value, the supply of the current is stopped by interlock. The limit is set as 20°C. Output laser power is controlled by input current. Relationship between input current and output power is shown in Figure 3.3, which is measured by power meter (COHERENT Inc. LM-5000). Resolution of the power meter is 1 W.

Table 3.2 Specification of semiconductor laser

Maximum power	250 W
Wavelength	980 nm
FWHM	3 nm
Fiber Φ	400 μm
Fiber NA	0.22

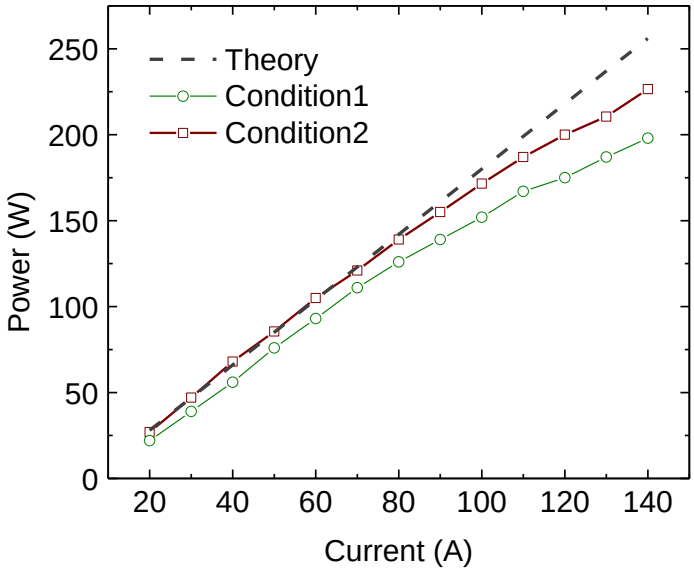

Figure 3.3 Relationship between input current and output power

Unfortunately, laser power has been lower than original value and its cause is not clear. Periodic maintenance is strongly required. In this thesis, experiment with sample holder type one and type two is conducted in condition one and two. The condition was improved slightly without any action in winter. The reason is guessed that high humidity made something trouble with laser.

3.3 Beam collimator

Laser radiation is fed through a multi-mode fiber and irradiated by a reflective collimator (THORLABOS Inc. RC04SMA-P01). Effective focal length (EFL) is 15 mm. Output beam diameter is described as following

$$\mathrm{Output\,Diameter} = 2 \times \mathrm{NA\,(Fiber)} \times \mathrm{EFL}\,. \tag{3.1}$$

Connected fiber NA is 0.22. Estimated output diameter is 6.6 mm. Optimum divergence angle of Gaussian beam is related to propagated distance as following.

$$\theta = \frac{\lambda}{\pi W_0}\,. \tag{3.2}$$

Here W_0 is beam waist radius and λ is wavelength. Propagated distance of this system is around 0.6 m. Estimated beam waist radius is 6.71 mm at the place where sample holder is set.

Because this collimator is not designed for high power laser, it is mounted in water cooled cupper, shown in Figure 3.4.

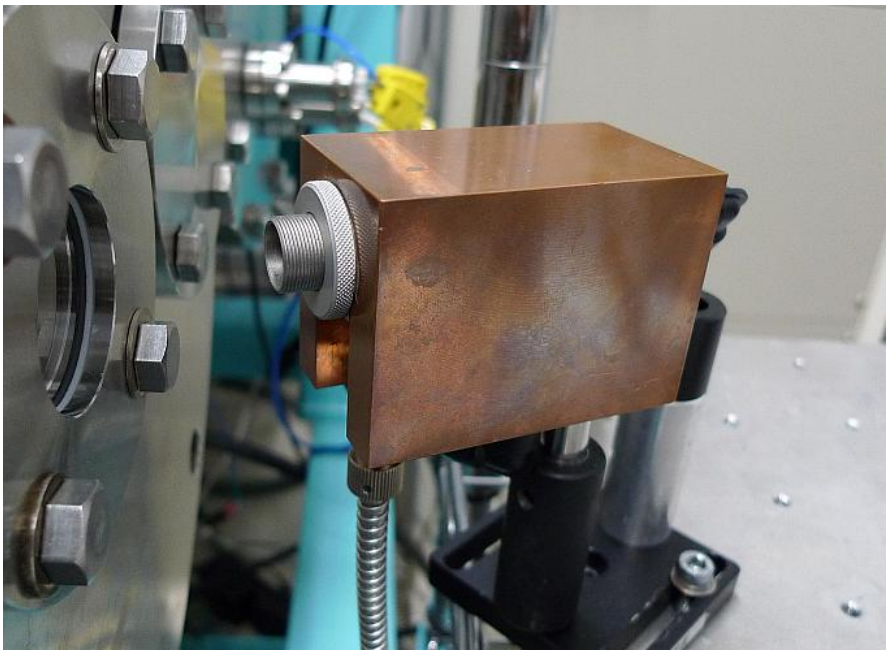

Figure 3.4 Photograph of the collimator and water cooled cupper

3.4 Power loss of installed laser

After transmission of whole light pass, total laser power is decreased by thermal loss of collimator and reflection on the quartz window. Second one is constant rate, 7 % of transmitted laser power but first one become larger in proportion to the increase of the laser power. The maximum total power loss is 25 %. When the experiment is being conducted, only reflected from the quartz window is measured. Thus input laser power is determined by comparing reflected power with measured power in vacuum chamber which is included whole power loss. Relationship between reflected power and measured power in vacuum chamber is shown in Figure 3.5.

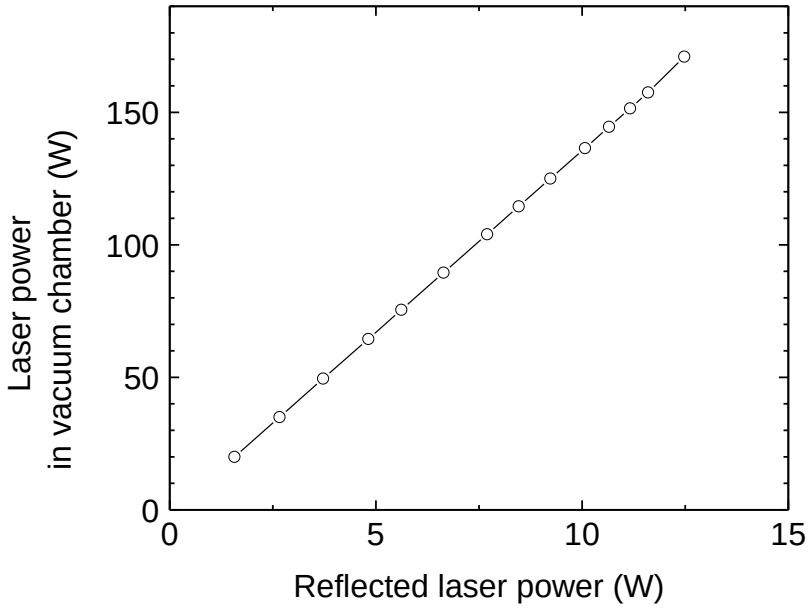

Figure 3.5 Relationship between reflected power and measured power in vacuum chamber

3.5 Measurement setup of XBSAS

Figure 3.6 shows the experimental setup. An external cavity diode laser was used as light source. In this experiment, the target absorption line is the transmission from metastable argon which corresponds with 772.37 nm. The laser wavelength was swept at the repetitive frequency of 0.1 Hz with the sweeping width of 10 GHz so as not to be distorted by a low pass filter in the lock-in amplifier. The laser is divided into the saturating beam and others. The saturating beam was

modulated with an acousto-optic modulator (AOM, 1205C; Isomet Corp.) and introduced into the optical fiber. The laser power at the output of the fiber is 1.2 mW and the laser spatial width at the measurement point was 0.8 mm at the crossing point. The fiber coupler is mounted at the upper side of chamber. The probe beam is coupled into the fiber and introduced to the chamber. The diameter is 0.8 mm at the crossing point and the power is 18 μW. The diameter of the laser is measured with beam profiler (SP503U; Ophir Optronics Solutions Ltd.). The evacuation of chamber may misalign the two beams. The probe beam was mounted on the optical table and was not displaced by the evacuation. The saturating beam was mounted on a flange. The flange moves down during the evacuation because an o-ring between chamber and window is squashed. This displacement can be compensated by mounting the saturating beam near the window and by putting a load to make the displacement vertical. The transmitted probe beam is divided into two beams. One is detected by PD2 (DET100; Thorlab Inc.) as a reference signal. This signal gives LAS result and is used for the evaluation of the line-integrated absorption signal. The other is detected by PD1 and the output of it is connected with a lock-in amplifier (LIA, SR830; Stanford Research Systems Inc.). This is for XBSAS. The pulse wave signal for AOM controller is used as a reference of LIA. The output of LIA is recorded with the oscilloscope.

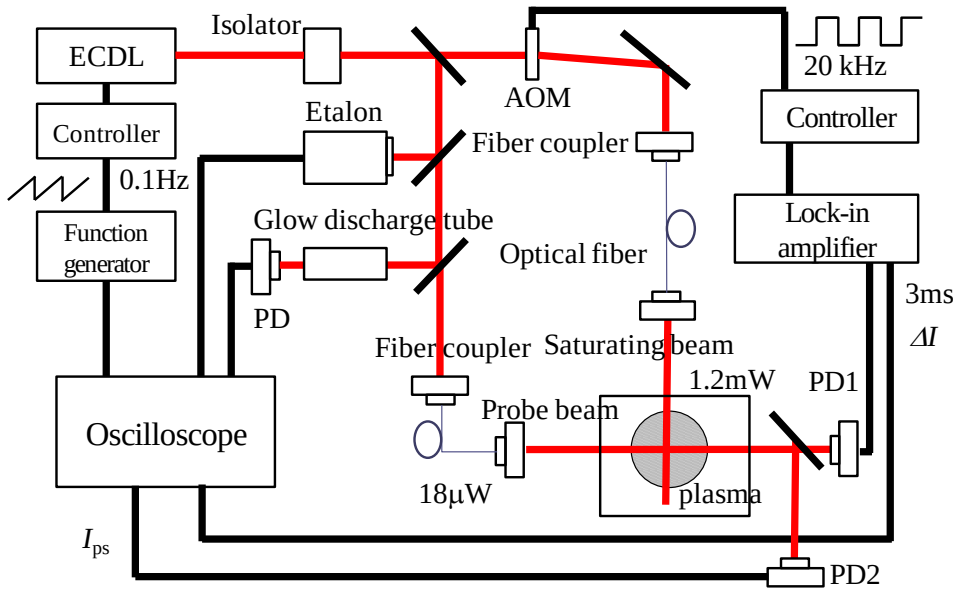

Figure 3.6 Experimental setup of XBSAS

3.6 Arc-heated plasma wind tunnel

The cross-sectional view and the operational conditions of the arc-heated plasma wind tunnel are shown in Figure 3.7 and Table 3.3 respectively. Using a conical nozzle with a throat diameter of 2 mm and a nozzle exit diameter of 30 mm, the flow inside this constricted arc heater is accelerated. This study is the first step of conduction the laser heating system, so that argon is used for working gas to simplify experiments. The volume flow rate of argon was 4 slm and the chamber pressure was 34.7 Pa. The vacuum system consists of two series of rotary pump and mechanical booster pump. The sample holder is fixed at 30 mm downstream of the nozzle exit.

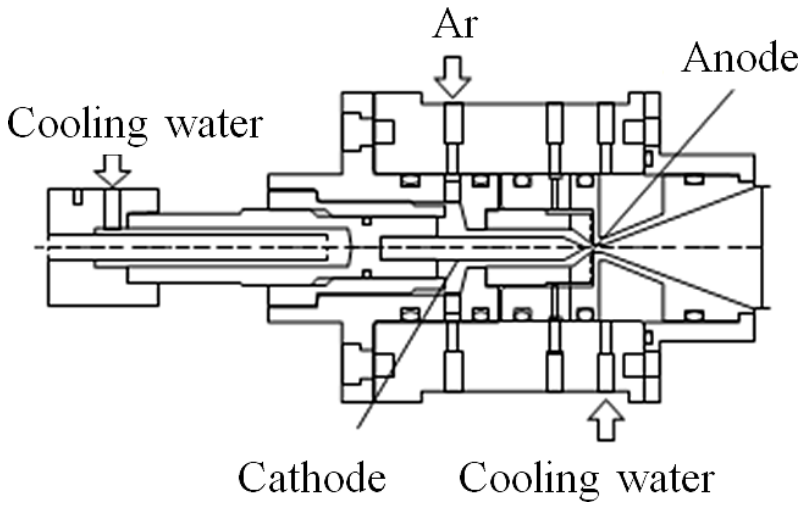

Figure 3.7 Schematic of the arc-heater

Table 3.3 Operational conditions of the arc-heated plasma wind tunnel

Parameter, unit	**value**
Current, A	80
Input power, kW	1.8
Specific enthalpy, MJ/kg	2.44
Nozzle exit diameter, mm	30
Mass flow rate of Ar, slm	4
Chamber pressure, Pa	34.7

3.7 Sample holder

Figure 3.8 shows the schematic of a flat-faced cylindrical sample holder. A test sample is a thin circular disk. In this study, two sample holders with same structure are made by referring to the JAXA's model[30]. First, holder 1 whose diameter is 35 mm is tentatively made. By using holder 1, three type of samples were tested, SiC, carbon composite (C/C) and alumina (Al_2O_3) for emissivity comparison. The emissivity is around 0.8, 0.8, 0.3 respectively. Then, as discussed in chapter 4 higher surface temperature, above 2000 K, is expected to be achieved on SiC sample with a small sample holder. Therefore, holder 2 whose diameter is 20 mm is designed and made by Tech volante Inc. Changes from holder 1 are 1) the whole scale, 2) material of the cover part, 3) fixing method of the holder cover. First, whole scale is reduced from holder 1. Second, material of the cover part is changed to silicon nitride (Si_3N_4) from SiC. Both materials are silicon-based ceramics and their physical properties are almost same. The biggest difference is thermal conductivity; 27 W/m/K for Si_3N_4 and 150 W/m/K for SiC. It means that thermal loss by heat transfer to the new holder should be smaller than to the holder 1 and expected surface temperature increases. Third, fixing method of the holder cover is changed. Unfortunately, cover of holder 1 was broken when a SiC sample was tested with high input laser power. The dominant cause of this accident is considered as fractures of connection part. The cover of holder 1 is fixed to a rear cupper part by mutual fitting with small pins. When the cover is removed, fixing hall part of the cover is fractured because of difficulty in disassembling. To avoid making fracture, the holder 2 has no small halls and is fixed by two cupper prates. Schematic of this configuration is shown in Figure 3.9 and specification of two sample holders are listed in Table 3.4.

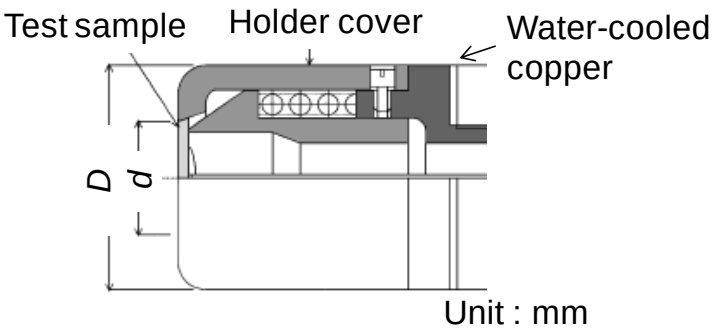

Figure 3.8 Schematic of a sample holder

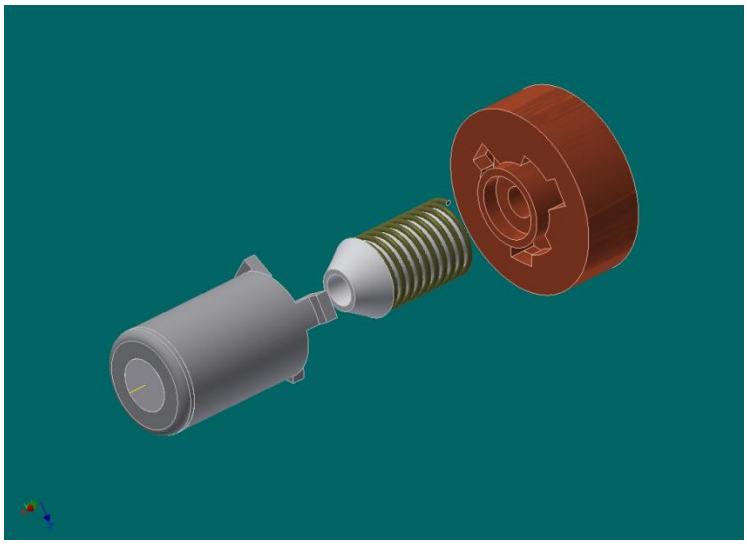

Figure 3.9 Schematic of the configuration of sample holder 2

Table 3.4 Specification of sample holders

Parameter, unit	**Holder 1**	**Holder 2**
Holder diameter *D*, mm	35	20
Sample diameter *d*, mm	15	10
Sample thickness, mm	3.5	2.5
Sample materials	SiC, C/C, Al_2O_3	SiC
Cover material	SiC	Si_3N_4

Chapter 4 SURFACE TEMPERATURE MEASUREMENT IN AN ARC-HEATED PLASMA WIND TUNNEL

4.1 Surface temperature estimation by measured emission spectrum

Figure 4.1 shows a plot of a theoretical curve-fitting and radiation spectrum of sample surface that was heated by laser and plasma flow. To carry out the fitting on the emission spectrum with the plasma flow, strong emissions from Ar I were cut. Comparison of input laser power with intensity of observed spectra of C/C sample is shown in Figure 4.2. When the intensity of Planck radiation is low, standard error of fitting increases due to the recombination radiation and bremsstrahlung of the plasma flow. In this study, when the standard error is over 5 %, temperature is considered as overestimated. In that case, temperature is estimated by the spectrum of the moment the arc-heater was turned off. Especially in the test of Al_2O_3, all measurements are conducted when the arc-heater was turned off because the radiation is quite low due to low emissivity. All measurements were conducted after three minutes of heating. The relationship between operation time and measurement time is discussed in Appendix 3.

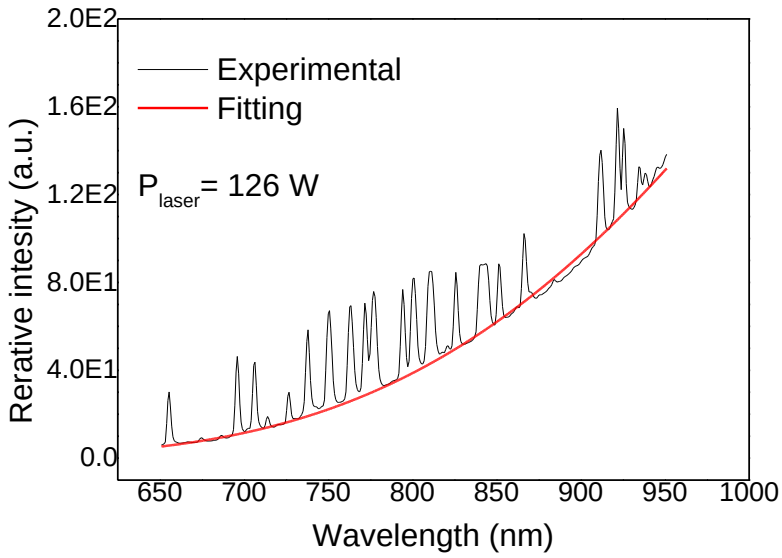

Figure 4.1 Typical measured emission spectrum from the sample surface

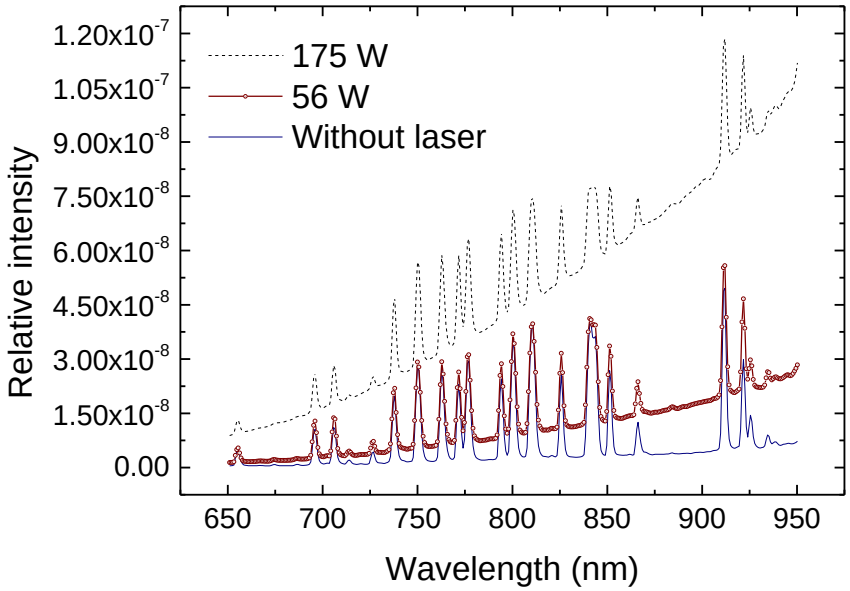

Figure 4.2 Comparison of measured spectra with and without laser heating

4.2 Measurement results

Surface temperatures of three samples were controlled by using laser without any change of flow condition. Measured surface temperatures of three samples with holder 1 are shown in Figure 4.3. A horizontal axis and vertical axis represent the input laser power and measured surface temperature. The point where input laser power is zero means that the sample is heated by only plasma flow. The maximum surface temperature was up to around 1600 K for SiC and C/C and 1900 K for Al_2O_3, respectively. Data series of SiC and C/C are quite similar but lower than Al_2O_3. The reason of this is that in this system thermal radiation has larger proportion to the total thermal loss than heat transfer to sample holder. It means that materials which have lower emissivity tend to be heated up to higher temperature. In low laser power region of SiC and C/C, temperature is not determined with plasma flow because standard error of fitting is larger than 5 %. To identify the difference between surface temperatures measured by spectrum including plasma flow and not, surface temperatures of SiC were measured by two conditions where arc heater is turned on and off. With plasma flow the surface temperature is overestimated by 5.6 % at the lowest laser power and 1.5 % at the highest laser power. The overestimation caused by plasma flow is considered as ignorable because the standard error of fitting is higher than 3 %.

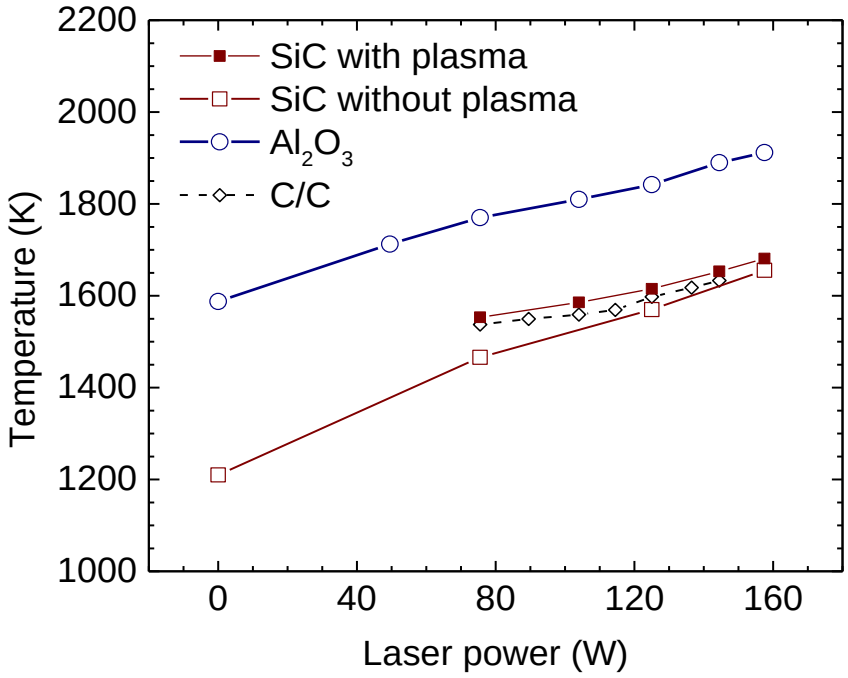

Figure 4.3 Measured surface temperatures of three samples

4.3 Comparison with theoretical value

4.3.1 Theoretical surface temperature estimation

Measured temperatures are compared with these theoretical values calculated in consideration of balance of heat transfer and input heating rate as seen in Figure 4.4. Heat transfer was calculated by Fourier's law assuming one-dimensional transfer to sample holder and thermal radiation loss is calculated by Stefan-Boltzmann law. The theoretical temperatures are obtained assuming that the calculated heat transfer is equal to heating rate of plasma flow q_s and heating rate of laser q_{laser} expressed as follows.

$$q_{trans} = q_s + q_{laser} - \varepsilon\sigma T_1^4 - \frac{S_2}{S_1}\varepsilon\sigma T_2^4 \tag{4.1}$$

q_{trans}, S, T, ε, and σ respectively denote heating rate of heat transfer, surface area, surface temperature, emissivity, and Stefan–Boltzmann constant.

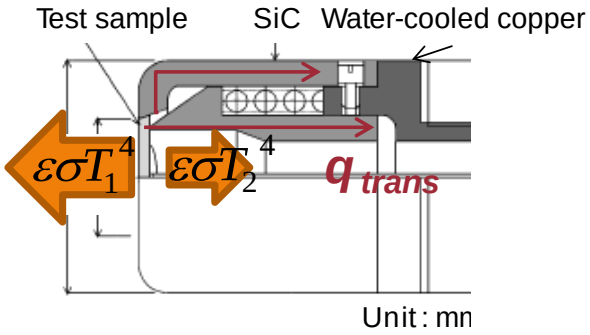

Figure 4.4 Schematic of surface temperature calculation

The heating rate of Argon plasma flow is calculated using an empirical equation reported by NASA[31].

$$q_s = \sqrt{\frac{p_s}{R_{eff}}} K_i \left(H_s - H_w \right) \tag{4.2}$$

H_s, H_w, p_s, and R_{eff} is the stagnation-point enthalpy, wall enthalpy, stagnation-point pressure, and effective nose radius. K_i is a specific constant given for test gas species. The detailed parameters which were used in this calculation are shown in Appendix 2.

4.3.2 Comparison of measured and estimated surface temperature

Figure 4.5 shows the comparison measured with estimated surface temperature of SiC and Al_2O_3. There are differences between measured and estimated surface temperature but tendency is same. The difference for Al_2O_3 is larger than SiC. A major cause of the large difference is considered that estimated heating rate of plasma flow is not correct. Figure 4.6 shows the comparison of measured surface temperature of Al_2O_3 with different input power of the arc heater. In this case input current 80 A is constant and this small difference of input power is uncontrolled. Therefore data series are not completed but it is obvious that small variation of input power lead to variation of surface temperature. On the other hand, variation of surface temperature for SiC is negligible small. The reason of this is because of the difference of emissivity. For high emissivity materials, heating rate of laser is larger than of plasma flow but for low emissivity materials it is opposite.

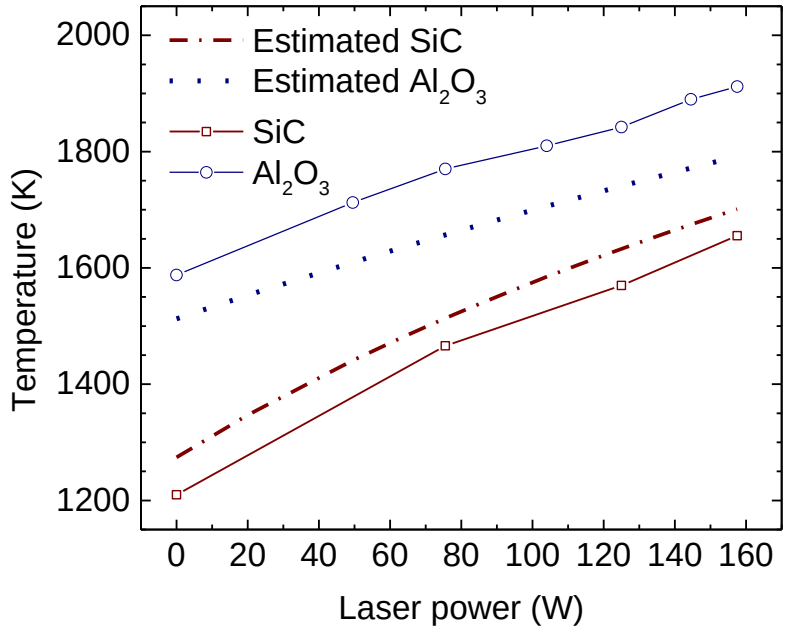

Figure 4.5 Comparison of measured and estimated surface temperature of SiC and Al_2O_3

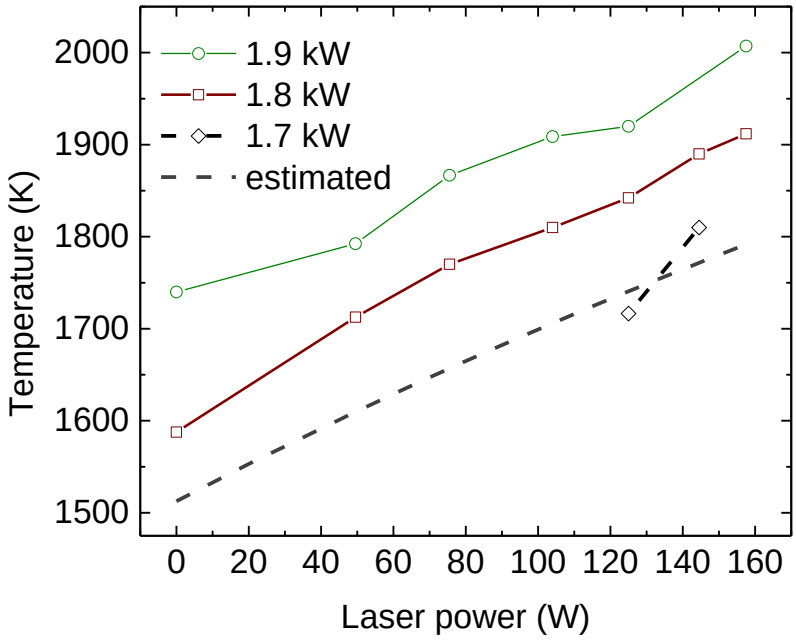

Figure 4.6 Comparison of measured surface temperature of Al_2O_3 with different input power of the arc heater

4.3.3 Method of achieving higher surface temperature for SiC

In arc-heated wind tunnel, oxygen partial pressure is expected to be up to several kilo pascal. To study the A/P-T condition of SiC, higher surface temperature above 2000 K is required. Thus how to achieve higher surface temperature for SiC is discussed here. From the comparison measured with estimated surface temperature, it is found that thermal radiation is dominant in thermal loss of higher emissivity materials. It means that decreasing the sample diameter is effective way to increase the surface temperature. Surface temperature of SiC with two holders are estimated and plotted in Figure 4.7. As the diameter of the holder is smaller, the higher temperature, above 2000 K, is expected to be obtained.

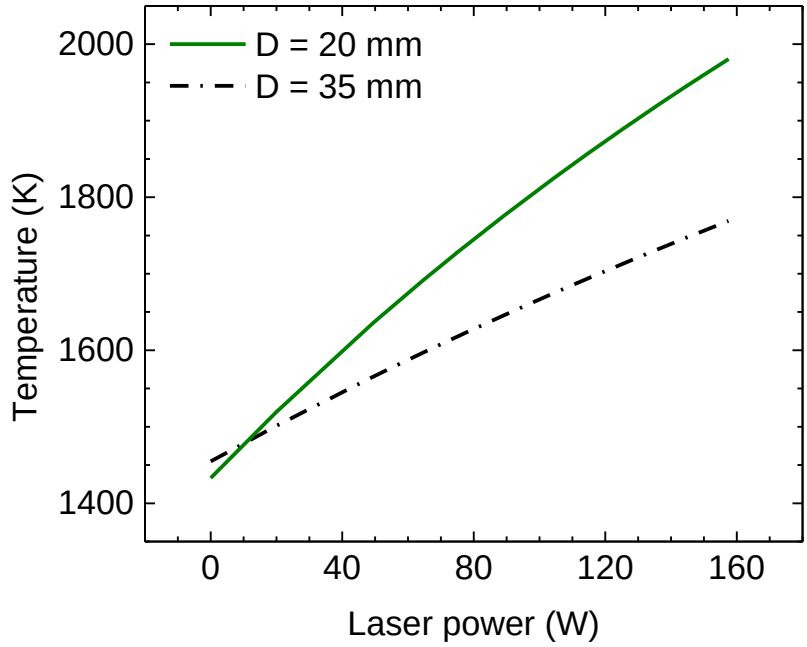

Figure 4.7 Comparison estimated surface temperature with different holder diameter

4.4 Measured surface temperature of SiC with small sample holder

Figure 4.8 shows the measured surface temperature of SiC with the holder 2. Measured surface temperature has good agreement with estimated surface temperature. The maximum surface temperature was up to 2165 K. The purpose of the holder 2 is accomplished. The error bars are obtained by three times measurement. The larger scattering in high laser power region, above 120 W, is caused form the fluctuation of input power of the heating laser.

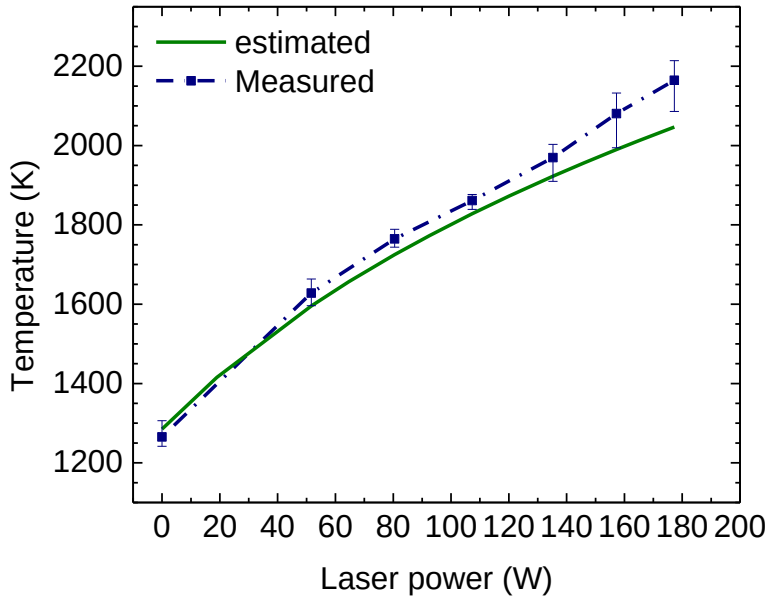

Figure 4.8 Measured and estimated surface temperature with holder diameter D = 20 mm

Chapter 5 TRANSLATIONAL TEMPERATURE DISTRIBUTION MEASUREMENT IN SURFACE-TEMPERATURE-CONTROLLED SHOCK LAYER

5.1 Generation of shock layer in front of sample holder

The shock layer was generated with the holder 2. The measurement point was fixed at 30 mm away from the nozzle exit. Figure 5.1 is the photograph of the sample holder in the flow. The probe laser diameter was 0.8 mm at the crossing point. The refraction effect of laser beam at the shock wave is negligibly small, and the alignment of two beams was not affected by the shock wave. The plenum and chamber pressures were respectively about 60 kPa and 35 Pa. Mach number of the flow was deduced as 2.27±0.05 by LAS using Equation (5.1) with $\gamma = 5/3$ and $R = 207$ J/kgK, while the designed Mach number is 2.

$$M = \frac{V}{\sqrt{\gamma R T_{\mathrm{tr}}}} \tag{5.1}$$

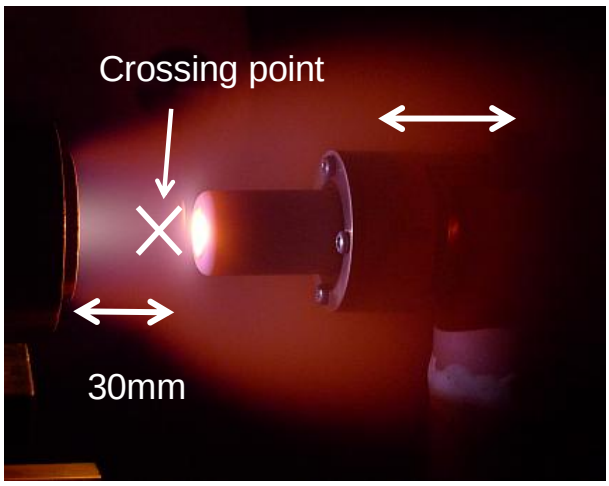

Figure 5.1 Photograph of the sample holder in the flow

Shock stand-off distance, Δd for a sphere probe was theoretically and experimentally estimated by several authors[32,33,34]. According to Lobb's approximation, the ratio of Δd to the probe diameter, D is approximately related to the ratio of density in the free stream to behind the shock wave as following for non-reacting flow

$$\frac{\Delta d}{D} \cong 0.41\left(\frac{\rho_2}{\rho_1}\right)^{-1}, \tag{5.2}$$

where

$$\frac{\rho_2}{\rho_1} = \frac{(\gamma+1)M_1^2}{(\gamma-1)M_1^2+2}. \tag{5.3}$$

Here, Δd is estimated at 4.9 mm by Equation (5.2) with M_1=2.27 and D=20 mm.

5.2 Results and discussions

The difference between unsaturated and saturated absorption coefficient was calculated by Equation (2.24). The measured XBSAS profile in Figure 5.2 was well fitted by Gaussian function.

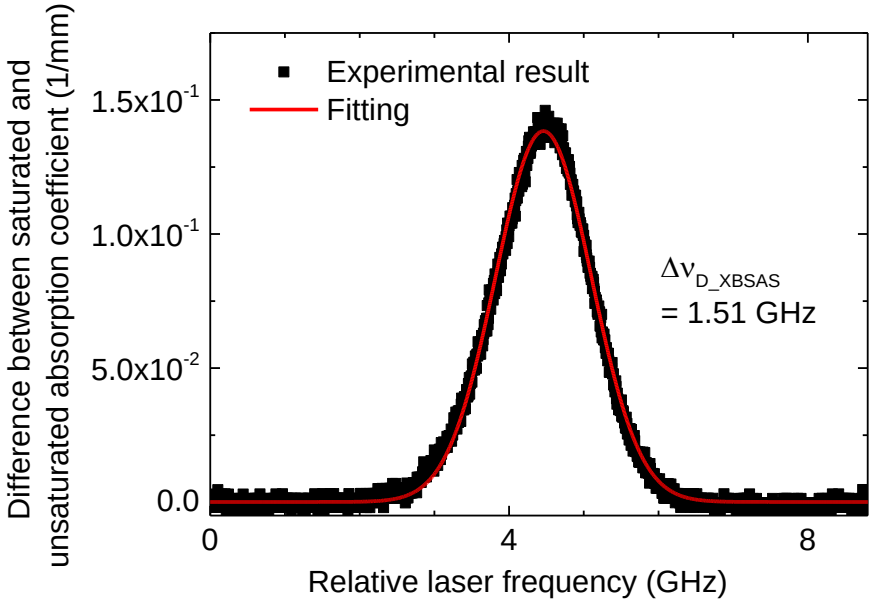

Figure 5.2 Typical signal of saturated absorption coefficient.

The translational temperature distribution along the stagnation streamline is shown in Figure 5.3. The measurement was conducted with and without laser heating. Input power of the heating laser was 171 W. The point 0 mm means the sample surface and the surface temperature is measured by emission spectroscopy as described above chapter. Measured surface temperature of the sample is

1200 K and 1700 K respectively with and without laser. In this facility, the mean free pass, λ was about 2 mm, and the plasma flow is in the transition region from the continuous flow to free molecular flow (Kn = 0.1~1). Thus the temperature jumped slowly from free stream to the shock layer. The peak temperature was 6400±500 K at x = 3 mm. With the free stream temperature and Mach number, the stagnation temperature was estimated to be over 6500±800 K, and the temperature measured by XBSAS is in reasonable agreement with it. Although the peak temperature of both case are almost same, the manner of temperature decrease from the peak to the sample surface is slightly different. This result suggests that the state in shock layer is affected by the surface temperature. This is the first demonstration of translational temperature measurement in the shock layer with changing surface temperature. This result should be compared with and validated by other methods or numerical simulations.

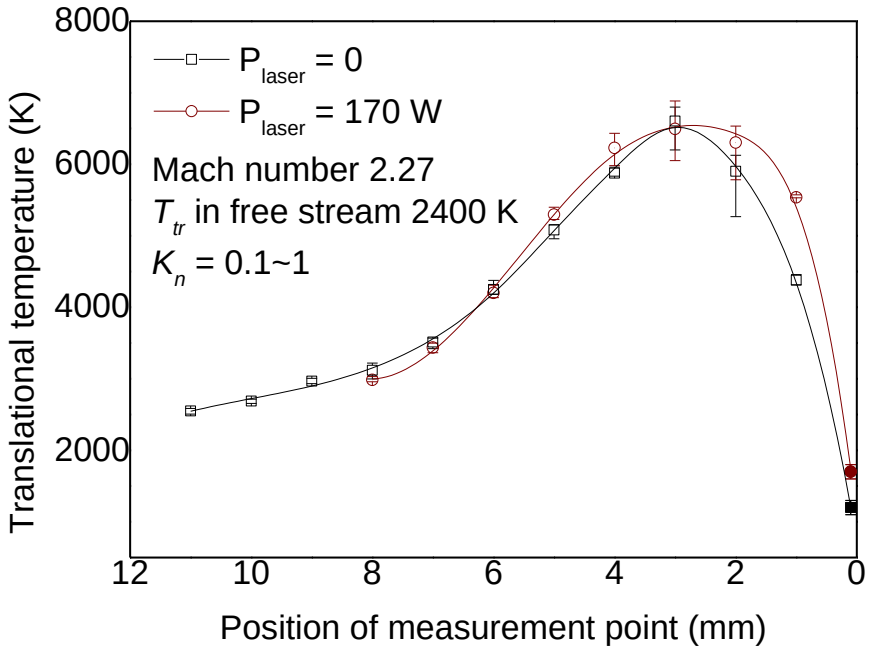

Figure 5.3 The translational temperature distribution along the stagnation streamline

Chapter 6 CONCLUSION

External heating system using semiconductor laser was installed in 1 kW-crass arc-heated wind tunnel and appropriate sample holder was designed for SiC test. Surface temperatures with two sample holder were measured by emission spectroscopy. The distributions of translational temperature in front of a sample holder with or without heated by laser were deduced by XBSAS. From the results obtained in these experiments, following are conclusions.

1. By using laser heating system, the surface temperature of a sample holder was controlled independently from argon plasma flow condition in arc-heated wind tunnel test. To design an appropriate sample holder which can reach high temperature, above 2000 K, the surface temperature was calculated considered the heat loss by thermal radiation and one-dimensional heat transfer to a sample holder. The calculation showed that diameters of sample and holder were important parameters. With a small sample holder whose diameter is 20 mm, the surface temperature of SiC was 1265 K in argon plasma flow and heated up to 2165 K by adding laser and it shows good agreement with calculated surface temperatures. Moreover, three materials that have different emissivity were tested. From the comparison among these results, this laser heating system is more effective for high emissivity materials than low emissivity materials.

2. The distributions of translational temperature in shock layer generated in front of the sample holder with and without laser heating were deduced by XBSAS. The peak temperature was observed at 3 mm in front of the sample holder and showed reasonable agreement with the estimated stagnation temperature. In both case, the distributions showed similar shape from the point where temperature start to increase to the peak, but between the peak and sample surface the shapes were slightly different. It means the surface temperature affects the shock layer. This distribution measurement is expected to be helpful not only to figure out the gas condition around a specimen during TPS test, but also to reveal the structure of the shock layer which is merged with thermal boundary layer.

References

[1] Howe, J., "Hypervelocity Atmospheric Flight: Real Gas Flow Field," NASA, TM101055, 1989.

[2] Yamada, T., Inatani, Y., Honda, M., & Hirai, K. I., "Development of thermal protection system of the MUSES-C/DASH reentry capsule," *Acta Astronautica*, vol. 51, 2002, pp. 63-72.

[3] Löhle, S., Mezger, A., & Fulge, H., "Measuerd surface temperatures of the Hayabusa capsule during re-entry determined from grond observation," *Acta Astronautica*, vol. 84, 2013, pp. 134-140.

[4] Arrington, James P. & Jones, Jim J., *Shuttle Performance: lessons learned*.: NASA Langley Research Center CP-2283 Part 2.

[5] Davies, C., & Arcadi, M., "Planetary Mission Entry Vehicles Quick Reference Guide. Version 3.0.," NASA/SP-2006-3401, 2006.

[6] Bernhard, R. P., Christiansen, E. L., Hyde, J., & Crews, J. L., "Hypervelocity impact damage into space shuttle surfaces," *International journal of impact engineering*, vol. 17, 1995, pp. 57-68.

[7] Auweter-Kurtz, M., & Wegmann, T., "Overview of IRS plasma wind tunnel facilities," STUTTGART UNIV (GERMANY FR) INST FUERRAUMFAHRTSYSTEME., 2000.

[8] Smith, R. K., Wagner, D. A., & Cunningham, J., "A survey of current and future plasma arc-heated test facilities for aerospace and commercial applications," *AIAA Paper*, vol. 36, 1989, pp. 98-0146.

[9] Momozawa, A., Taubert, S., Nomura, S., Komurasaki, K., & Arakawa, Y., "Nitriding of zirconium cathode for arc-heater testing in air," *Vacuum*, vol. 85, 2010, pp. 591-595.

[10] Munk, M. M., Glaab, L., Samareh, J., & Agrawal, P. , "MULTI-MISSION EARTH ENTRY VEHICLE DEVELOPMENT BY NASA'S IN-SPACE PROPULSION TECHNOLOGIES (ISPT) PROJECT," *In 9th International Planetary Probe Workshop*, 2012.

[11] Gasch, M., & Johnson, S., "Physical characterization and arcjet oxidation of hafnium-based ultra high temperature ceramics fabricated by hot pressing and field-assisted sintering," *Journal of the European Ceramic Society*, vol. 30, 2010, pp. 2337-2344.

[12] Gasch, M., Ellerby, D., Irby, E., Beckman, S., Gusman, M., & Johnson, S. , "Processing, properties and arc jet oxidation of hafnium diboride/silicon carbide ultra high temperature ceramics," *Journal of Materials Science*, vol. 39, 2004, pp. 5925-5937.

[13] Savino, R., De Stefano Fumo, M., Paterna, D., Di Maso, A., & Monteverde, F. , "Arc-jet testing of ultra-high-temperature-ceramics," *Aerospace Science and Technology*, vol. 14, 2010, pp. 178-187.

[14] Wernitz, R., Eichhorn, C., Marynowski, T., & Herdrich, G., "Plasma Wind Tunnel Investigation of European Ablators in Nitrogen/Methane Using Emission Spectroscopy," *International Journal of Spectroscopy*, 2013.

[15] Morino, Y., Yoshinaka, T., Auweter-Kurtz, M., Hilfer, G., Speckmann, H. D., & Sakai, A., "Erosion characteristics of SiC coated C/C materials in arc-heated high enthalpy air flow," *Acta Astronautica*, vol. 50, 2002, pp. 149-158.

[16] Monteverde, F., Savino, R., Fumo, M. D. S., & Di Maso, A., "Plasma wind tunnel testing of ultra-high temperature ZrB2–SiC composites under hypersonic re-entry conditions," *Journal of the European Ceramic Society*, vol. 30, 2010, pp. 2313-2321.

[17] Ogasawara, T., Ishikawa, T., Yamada, T., Yokota, R., Itoh, M., & Nogi, S. , "Thermal response and ablation characteristics of carbon fiber reinforced composite with novel silicon containing polymer MSP," *Journal of composite materials*, vol. 36, 2002, pp. 143-157.

[18] Narushima, T., Goto, T., Hirai, T., & Iguchi, Y., "High-temperature oxidation of silicon carbide and silicon nitride," *Materials Transactions, JIM*, vol. 38, 1997, pp. 821-835.

[19] Kubota, Y., Hatta, H., Yoshinaka, T., Kogo, Y., Goto, T., & Rong, T., "Use of Volume Element Methods to Understand Experimental Differences in Active/Passive Transitions and Active Oxidation Rates for SiC," *Journal of the American Ceramic Society*, vol. 94, 2013, pp. 1317-1323.

[20] Hinze, J. W., & Graham, H. C., "The Active Oxidation of Si and SiC in the Viscous Gas‐Flow Regime," *Journal of the Electrochemical Society*, vol. 123, 1976, pp. 1066-1073.

[21] Mizuno, M., Ishida, K., Ito, T., Kurotaki, T., & Matsuzaki, T., "Oxygen Recombination Coefficient on Catalytic Surfaces in Ar-O 2 Inductively Coupled Plasma by Actinometry," *TRANSACTIONS OF THE JAPAN SOCIETY FOR AERONAUTICAL AND SPACE SCIENCES*, vol. 49, 2006, pp. 49-54.

[22] Balat, M., Flamant, G., Male, G., & Pichelin, G., "Active to passive transition in the oxidation of silicon carbide at high temperature and low pressure in molecular and atomic oxygen," *Journal of materials science*, vol. 27, 1992, pp. 697-703.

[23] Nomura S., "High Sensitive and Point-Measurement Laser Absorption Spectroscopy of High Enthalpy Flow," The University of Tokyo, Doctoral dissertation 2013.

[24] Yamada, T., & Inatani, Y., "ISAS High Enthalpy Flow Facility for Thermal Protection Material Tests," *Proceedings of 26th IEPC*, 1999, pp. 1362-1369.

[25] Yamada, T., Ishida, Y., Suzuki, T., Takasaki, K., Fujita, K., Ogasawara, T., & Abe, T., "Development of high and low density ablators for dash-ii and future reentry missions," *TRANSACTIONS OF THE JAPAN SOCIETY FOR AERONAUTICAL AND SPACE SCIENCES, AEROSPACE TECHNOLOGY JAPAN*, vol. 8, 2010, pp. 61-69.

[26] Matsui M., "Application of Laser Absorption Spectroscopy to High Enthalpy Flow Diagnostics," The University of Tokyo, Doctral dissertation 2005.

[27] Ida, T., Ando, M., & Toraya, H., "Extended pseudo-Voigt function for approximating the Voigt profile," *Applied Crystallography*, vol. 33, 2000, pp. 1311-1316.

[28] J. Végh, "Alternative form for the pseudo-Voigt peak shape," *Review of Scientific Instruments*, vol. 76, 2005, p. 056107.

[29] Matsui, M., Komurasaki, K., Ogawa, S., & Arakawa, Y., "Influence of laser intensity on absorption line broadening in laser absorption spectroscopy," *Journal of applied physics*, vol. 100, 2006, p. 063102.

[30] T. Kurotaki, "Precise Method to Estimate Aerodynamic Heat on Reentry Vehicles while Atmospheric Reentry," *NAGARE. The JSFM*, vol. 22, 2003, pp. 477-484, in Japanese.

[31] Ernest. V., "Empirical Stagnation-Point Heat-Transfer Relation In Several Gas Mixtures at High Enthalpy Levels," NASA, TN D-799 1968.

[32] K. Hida, "An approximate study on the detached shock wave in front of a circular cylinder and a sphere," *Journal of ths Physical Society of Japan*, vol. 8, 1953, pp. 740-745.

[33] H. Olivier, "A theoretical model for the shock stand-off distance in frozen and equilibrium flows," *Journal of Fluid Mechanics*, vol. 413, 2000, pp. 345-353.

[34] Belouaggadia, N., Olivier, H., & Brun, R., "Numerical and theoretical study of the shock stand-off distance in non-equilibrium flows," *Journal of Fluid Mechanics*, vol. 607, 2008, pp. 167-197.

Appendix

A.1 Dependency on saturating beam intensity in XBSAS profiles

In XBSAS, the measured profile varies with the saturating beam intensity. Figure A.1 shows a ratio of FWHM of XBSAS profile, $\Delta\nu_{D\_XBSAS}$ to true profile as a function of saturation parameter which was obtained by Nomura. Saturation parameter is I/I_s.

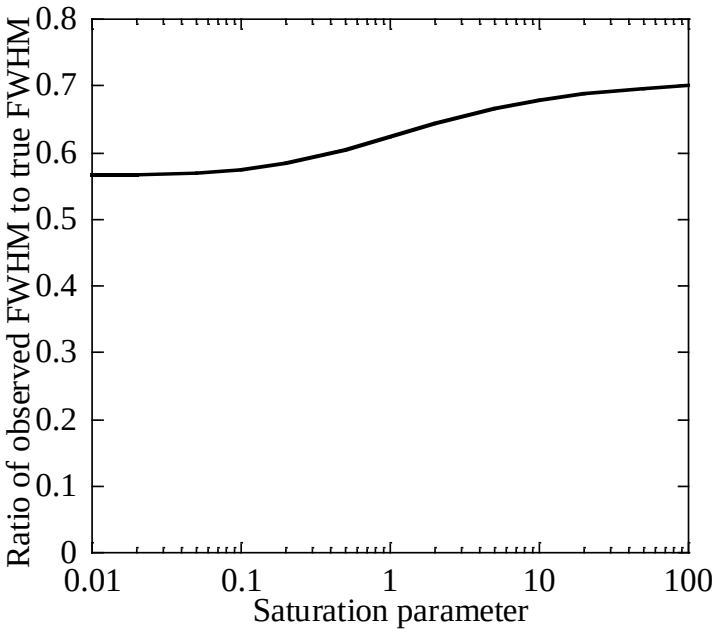

Figure A.1 Ratio of FWHM of the XBSAS profile to true profile as a function of saturation parameter [23]

In incompletely saturated region, Translational temperature is easily obtained by Equation (2.26). Once the saturation intensity is obtained, a ratio of $\Delta\nu_{D\_XBSAS}$ to $\Delta\nu_{D,}$ α is known by using the curve in Figure A.1. Saturated absorption was evaluated by LAS with changing the probe laser intensity. Measured saturated integrated absorbance and the fitting curve by Equation (2.15) are shown in Figure A.2. The saturation intensity was estimated at 0.064 mW in this study.

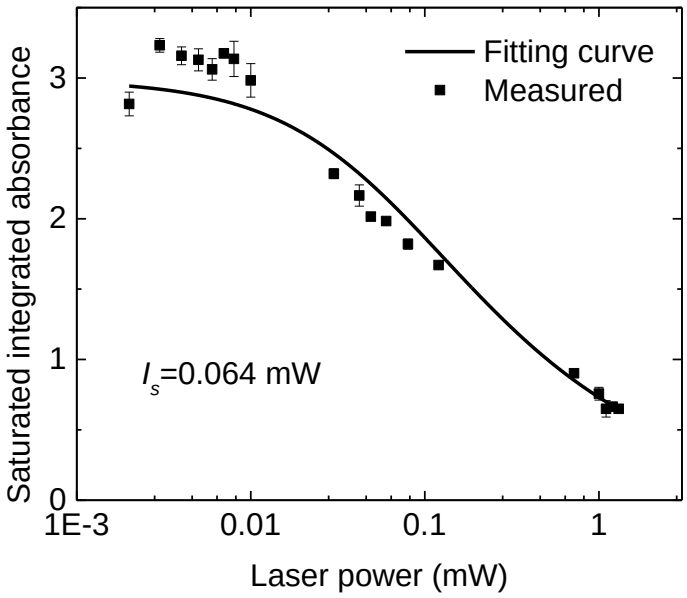

Figure A.2 Saturated integrated absorbance as a function of laser power

The saturating laser intensity is 1.2 mW, so that the saturation parameter is 18.75 and α is known as 0.69 in Figure A.1.

The saturation intensity should be modified from Equation (2.18). In XBSAS, the atoms which absorb the saturating and probe beams have a same velocity component in *x* and *y* directions. The Root-mean-square $\bar{v}$ is

$$\bar{v}(\nu)=\sqrt{\frac{2(\nu-\nu_0)^2}{\nu_0^2}c^2+\frac{k_B T_{tr}}{m}}\,. \tag{6.1}$$

The saturation intensity $I_s(\nu)$ is rewritten as

$$I_{cs}(\nu)=I_{cs}\sqrt{\frac{16\ln 2}{3}\frac{(\nu-\nu_0)^2}{\Delta\nu_D^2}+\frac{1}{3}}\,. \tag{6.2}$$

A.2 Physical properties and parameters of the surface temperature estimation

Thermal conductivities of SiC, Al_2O_3, Cu which were used for the calculation of the heat transfer are 150, 32, 401 W/m/K respectively.

Parameters for the calculation of the heating rate of Argon plasma flow by using Equation (4.2) are listed in Table A.1. Hear, H_s - H_w can be approximated as the specific enthalpy of free stream. By assuming frozen flow, the specific enthalpy of free stream can be approximated as $V^2/2$ Pitot pressure is obtained by chamber pressure, Mach number and γ. Argon is monoatomic molecule, so that γ is 5/3.

Table A.1 Parameters of the surface temperature estimation

Parameter, unit	**Value**
Mach number	2.27
Chamber pressure, Pa	34.7
Pitot pressure P_s, kPa	8.5
Heat capacity ratio γ	5/3
Free stream velocity V, m/s	2070
Specific constant K_i, $\frac{g}{cm^{3/2} \cdot sec \cdot atm^{1/2}}$	0.1744

A.3 Relationship between operation time and measurement time

The relationship between operation time and the surface temperature is examined with SiC and holder 2, shown in Figure A.3. Currents of input laser power source are written in the graph. In this operation, the laser power was gradually increased to the maximum power and then gradually decreased. In both step, the surface temperatures was close to constant in less than three minutes. There is a small difference between when laser power was increased and decreased. For instance, in the case of 100 A, the temperature when the laser power was increased and decreased were 2003 K and 2055 K, respectively. The estimated convergence temperature is 2025 K and the error is less than 2 %. In this study, this error is ignored and all operations were conducted by increasing laser power.

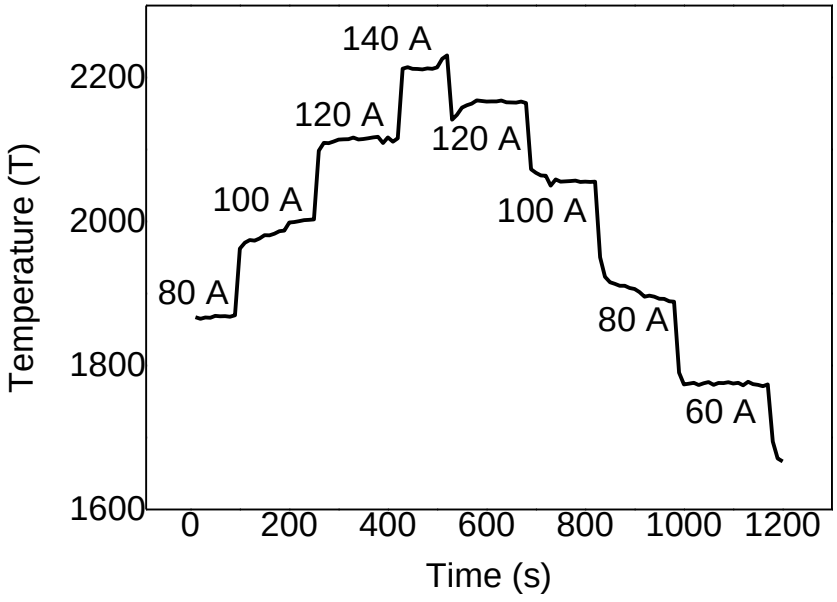

Figure A.3 The relationship between operation time and the surface temperature of SiC